Springer

Acta Mechanica Sinica

CrossMark click for updates

• RESEARCH PAPER •

Acta Mech. Sin., Vol. 38, 522140 (2022)
https://doi.org/10.1007/s10409-022-22140-x

# A forward-inverse dynamics modeling framework for human musculoskeletal multibody system

Xinyue Wang, Jianqiao Guo*, and Qiang Tian

*MOE Key Laboratory of Dynamics and Control of Flight Vehicle, School of Aerospace Engineering, Beijing Institute of Technology, Beijing 100081, China*

Received June 20, 2022; accepted July 15, 2022; published online August 11, 2022

Multibody musculoskeletal modeling of human gait has been proved helpful in investigating the pathology of musculoskeletal disorders. However, conventional inverse dynamics methods rely on external force sensors and cannot capture the nonlinear muscle behaviors. Meanwhile, the forward dynamics approach is computationally demanding and only suited for relatively simple tasks. This study proposed an integrated simulation methodology to fulfill the requirements of estimating foot-ground reaction force, tendon elasticity, and muscle recruitment optimization. A hybrid motion capture system, which combines the marker-based infrared device and markerless tracking through deep convolutional neural networks, was developed to track lower limb movements. The foot-ground reaction forces were determined by a contact model for soft materials, and its parameters were estimated using a two-step optimization method. The muscle recruitment problem was first resolved via a static optimization algorithm, and the obtained muscle activations were used as initial values for further simulation. A torque tracking procedure was then performed by minimizing the errors of joint torques calculated by musculotendon equilibrium equations and inverse dynamics. The proposed approach was validated against the electromyography measurements of a healthy subject during gait. The simulation framework provides a robust way of predicting joint torques, musculotendon forces, and muscle activations, which can be beneficial for understanding the biomechanics of normal and pathological gait.

**Multibody dynamics, Musculoskeletal modeling, Gait, Forward-inverse dynamics, Musculotendon dynamics**

**Citation:** X. Wang, J. Guo, and Q. Tian, A forward-inverse dynamics modeling framework for human musculoskeletal multibody system, Acta Mech. Sin. **38**, 522140 (2022), https://doi.org/10.1007/s10409-022-22140-x

## 1. Introduction

Human locomotion is driven and supported by the musculoskeletal system. It is made up of bones, skeletal muscles, joints, along with soft connective tissues, and all of them consist a typical multibody system. Human gait analysis via multibody dynamics simulations can obtain joint torques and muscle forces which are difficult to measure from experiments [1]. Multibody modeling of human musculoskeletal system provides a simulation platform for understanding the biomechanics of human locomotion, and it has broad applications in sports engineering [2], ergonomics [3-5], and clinical treatments [6-10].

However, musculoskeletal multibody simulation is a complex problem due to the nonlinearity originated from the dynamic equations of motion, muscle contraction dynamics, and foot-ground contact forces [1, 11]. The solution methods for the musculoskeletal models can be categorized into inverse and forward approaches. The inverse dynamics approach needs to use the measured joint kinematics and external forces as model inputs to calculate joint torques and muscle forces [12, 13]. By this means, human locomotion was assumed time-independent, and static optimization (SO) [14] was further adopted to solve the muscle redundancy problem. However, this assumption ignores the force equilibrium within the musculotendon unit and its contraction dynamics [15]. In addition, it is difficult to obtain the foot-ground reac-

*Corresponding author. E-mail address: guojianqiao@bit.edu.cn (Jianqiao Guo)
Executive Editor: Jian Xu

tion forces without force plates or plantar pressure measurement sensors [16]. The forward dynamics approach takes the neural commands acquired via electromyography (EMG) measurements [17-19] or controllers [20-24] as model inputs to calculate human body movements. Researchers have developed numerous dynamic optimization methods to minimize metabolic costs and kinematic errors [25, 26]. However, compared with inverse dynamics analysis, this method is computationally inefficient and thus difficult to apply to three-dimensional gait analysis.

Recently, researchers have tried to combine the forward and inverse dynamics approaches [27] to compromise accuracy and efficiency [28]. For example, Skipper Anderson et al. [29] provided the force-dependent kinematics method to determine the ligament forces within the non-conforming joints including the hip [30], knee [31], spine [32, 33], etc. However, this approach still cannot consider the musculotendon equilibrium equation [29]. Computed muscle control (CMC) [20, 34] is another forward-inverse coupling method that has been widely used by many researchers. However, according to Wesseling et al. [35], the moment tracking performance of the CMC method is poorer than SO. Shourijeh et al. [15] proposed a forward-muscular inverse-skeletal (FMIS) framework by solving the muscle redundancy problem via a torque tracking algorithm. They also developed forward static optimization (FSO) methods based on kinematic tracking [36]. However, the utilization of the FSO methods was still limited within the planar musculoskeletal systems with few degrees of freedom (DOFs) due to their low computational efficiency.

The forward-inverse coupling framework is feasible to be combined with the foot-ground contact model, providing the possibility to estimate the walking kinetics outside the laboratory. Based on the parameter identification method, one can obtain the ground reaction forces without force plates. For example, Pàmies-Vilà et al. [37] combined the parameter optimization strategy and the extended Kalman filter to predict human gait patterns, while the estimated tangential force results were not agreed with the experimental data. Shourijeh and McPhee [38] provided the hyper-volumetric contact model to consider the non-local contact behavior at the plantar soft tissues. Based on this model, a two-dimensional torque-driven gait model was developed by Ezati et al. [39], while this method cannot eliminate the residual loads on the pelvis imposed by motion constraints. Lopes et al. [40] simplified the foot-ground contact geometry as a super-ellipsoid to a plane, reducing the spatial resolution compared with point-to-plane contact models like Refs. [41, 42]. Recently, Van Hulle et al. [43] provided a foot-ground contact model that fits for inverse dynamics calculations, but its validity and reliability strongly depend on the accuracy of the landmarks attached to the feet. Therefore, how to combine a foot-ground contact model with muscle-driven gait models is still needed to be investigated.

In addition, the mixture of forward and inverse dynamics approaches enables some joint angles to be calculated rather than merely measured from experiments. These DOFs can use markerless motion capture data [44] as kinematic inputs, preventing the time-consuming tasks of attaching the reflective markers. Kinect-driven musculoskeletal models were developed by Skals et al. [45] and Hirano et al. [46], and these models can be used to evaluate the gait abnormalities of Parkinson's disease patients [47]. However, the accuracy of lower limb kinematics was low since only two virtual markers were attached to a rigid body segment. Moreover, the accuracy of the video-based markerless motion capture systems [48] can be improved by combining it with multibody kinematics calculation [49-51]. This hybrid motion capture method can be used to obtain the kinematic inputs of the musculoskeletal models.

This paper aims to provide a FMIS framework for calculating joint reaction torques and muscle forces. In Sect. 2, a hybrid motion capture system including eight infrared and four video cameras was established. Based on the measured kinematics data, we further optimized the ground reaction forces and then estimated the muscle recruitment patterns of the lower limb. To validate the presented modeling approach, the obtained data were compared against literature data and EMG measurements in Sect. 3. Section 4 further discussed the main findings and limitations of our research.

## 2. Methods

### 2.1 Experimental setup and procedures

#### *2.1.1 Gait kinematic analysis*

A healthy male subject (29 years, 175 cm, 59 kg) was selected in this study and signed informed consent before the experiment. The recruited subject reported no lower limb injuries within half a year and did not engage in strenuous exercise 48 hours before the experiment. This study has been approved by the ethics committee of Beijing Institute of Technology.

The subject performed one static calibration trial before gait testing. Then, he was instructed to walk at self-selected speed, see Fig. 1a. Based on a modified Helen Haynes marker arrangement [52], nineteen reflective markers were placed on the following anatomical landmarks: the left/right anterior superior iliac spine, the midpoint of the posterior superior iliac spine, the front side of the left/right thigh,

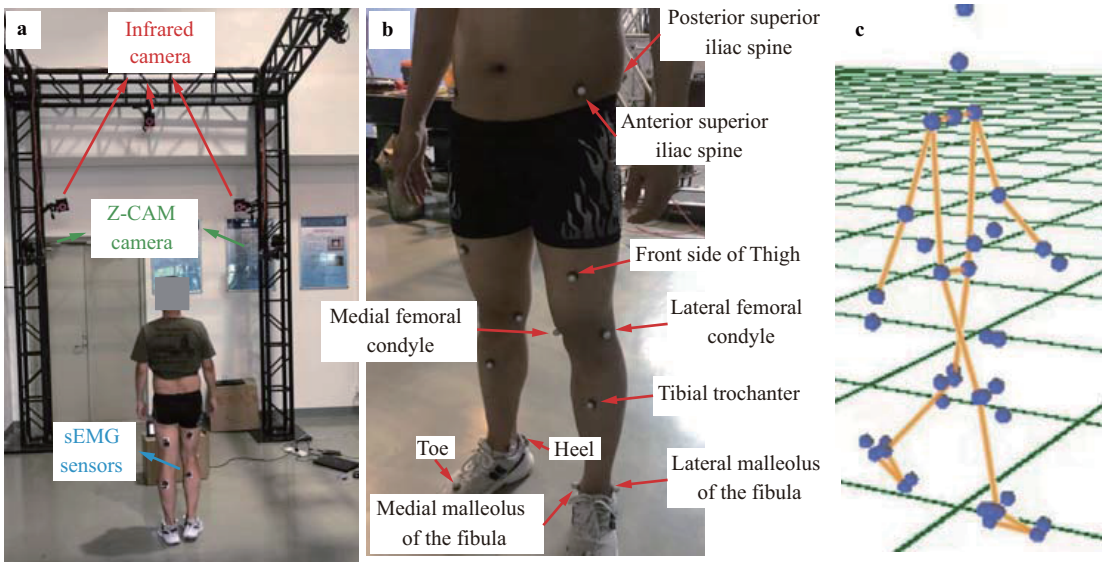


**Figure 1** Experimental setup and procedure. **a** Infrared-AI hybrid motion capture system; **b** modified Helen Haynes marker arrangement; **c** landmark positions obtained via hybrid motion capture system.

the left/right lateral femoral condyle, the left/right medial femoral condyle, the left/right tibial trochanter, the left/right lateral malleolus of the fibula, the left/right medial malleolus of the tibia, the left/right toe, and the left/right heel. As shown in Fig. 1a, motion data were collected synchronously using an eight-lens infrared motion tracking system (Nokov Tech., Beijing, China) and four Z-CAM cameras (ImagineVision Tech., Shenzhen, China) at a sample rate of 60 Hz. Both camera systems were calibrated simultaneously based on a L-frame calibration object.

Video data were processed using Fastmove software (Fast Move Tech., Dalian, China) to estimate the position of twenty-one anatomical landmarks of humans [53, 54]. The markerless pose estimation was accomplished using deep convolutional neural networks [55] trained on over 1200000 manually annotated digital images of human postures. The obtained virtual landmark positions were then transformed to the same global coordinate as that shared by the reflected markers, see Fig. 1c. The gait events were determined based on the position and velocity of the right heel marker [56].

To obtain the lower limb joint angles based on the markerless motion capture system, some kinematic assumptions were adopted [57, 58]. Here, the knee flexion angle was defined as the angle of intersection between the longitudinal axes of the thigh and the thank, without considering its adduction/abduction and external/internal rotation. The ankle joint was also simplified as a revolute joint. Its dorsiflexion was inclination angle between the shank and the foot. Moreover, the relative rotation between the pelvis and the lower trunk was neglected, and the pelvis reference frame $[\boldsymbol{i}_{\mathrm{LTK}},\ \boldsymbol{j}_{\mathrm{LTK}},\ \boldsymbol{k}_{\mathrm{LTK}}]$ was defined as [57]

$$\begin{aligned}&\boldsymbol{k}_{\mathrm{LTK}}=\frac{\boldsymbol{r}_{\mathrm{rh/lh}}}{\left\|\boldsymbol{r}_{\mathrm{rh/lh}}\right\|},\ \boldsymbol{j}_{\mathrm{LTK}}=\boldsymbol{k}_{\mathrm{LTK}}\times\frac{\boldsymbol{r}_{\mathrm{ms/mh}}}{\left\|\boldsymbol{r}_{\mathrm{ms/mh}}\right\|},\\&\boldsymbol{i}_{\mathrm{LTK}}=\boldsymbol{j}_{\mathrm{LTK}}\times\boldsymbol{k}_{\mathrm{LTK}}.\end{aligned}\tag{1}$$

Here, $\boldsymbol{r}_{\mathrm{rh/lh}}$ denotes the vector of the right hip joint center relative to the left one, and $\boldsymbol{r}_{\mathrm{ms/mh}}$ is the vector that connects the middle point of both shoulders and the intermediate landmark of both hips. For simplicity, the hip flexion was quantified by sagittal angle between the longitudinal axis of the thigh and $\boldsymbol{j}_{\mathrm{LTK}}$. The hip abduction angle corresponded to the inclination angle between the longitudinal axis of the thigh and $\boldsymbol{k}_{\mathrm{LTK}}$ in the coronal plane.

### 2.1.2 *Lower limb muscle activities*

During each gait trail, the activation patterns of lower limb muscles were synchronously measured via a 8-channel EMG system (Fast Move Tech., Dalian, China) using the sampling rate of 1000 Hz. Surface EMG data were collected from the gluteus maximus, gluteus medius, rectus femoris, vastus lateralis, biceps femoris, lateral gastrocnemius, and tibialis anterior muscles for the right leg. Moreover, the subject was asked to perform three repetitive trails of maximum voluntary contractions (MVCs) to obtain the maximal force-generating capabilities of each muscle group.

The EMG signals recorded during gait and MVC trails were first rectified and then band-pass filtered between 10 and 250 Hz [19]. After that, the smoothed EMG data were filtered using a 4-order Butterworth filter with a 6 Hz low-pass cut-off frequency [17]. The MVC value for each muscle was determined as the root mean square of the EMG signal in a 250 ms window [59]. To further acquire the linear envelope,

the EMG signals measured during gait tests were normalized by the obtained MVC. Finally, the obtained smooth signal, named muscular excitation level $u$, was used as the input of a first-order time delay differential equation to calculate the activation $a$ [60]:

$$\frac{\mathrm{d}a}{\mathrm{d}t} = \frac{u-a}{\tau_a(a,u)}, \tag{2}$$

where $\tau_a(a,u)$ has the mathematical form:

$$\tau_a(a,u) = \begin{cases} \tau_{\mathrm{act}}(0.5+1.5a), & u > a, \\ \tau_{\mathrm{deact}}/(0.5+1.5a), & u \le a, \end{cases}$$

and $\tau_{\mathrm{act}}$ and $\tau_{\mathrm{deact}}$ are the time constants for activation and deactivation, respectively.

## 2.2 Musculoskeletal modeling

The multibody musculoskeletal model included seven rigid bones and forty-three musculotendon units, see Fig. 2. The bone geometry was originated from generic database within the OpenSim gait2392 model [61]. It was then scaled based on the stick diagram reconstructed from the calibration in standing posture (Fig. 1c). Each bone segment was regarded as a rigid body ignoring the deformation caused by human locomotion [62]. The bone segment lumped the inertial properties of its surrounding muscle and connective tissue, and the mass and inertia values were scaled according to the subject's height and weight [63]. The human joint was described based on mathematical constraints, and the head-and-torso (HAT) model was assumed fixed to the pelvis. As a result, the gait model consisted of six DOFs for the pelvis, and five DOFs for each leg (hip flexion, abduction, rotation, knee flexion, and ankle flexion), see Fig. 2a. The range of motion of each rotational DOF was limited by a torsional spring [64, 65], reflecting the passive stiffness of ligaments, joint capsules, and other soft tissues surrounding the joint.

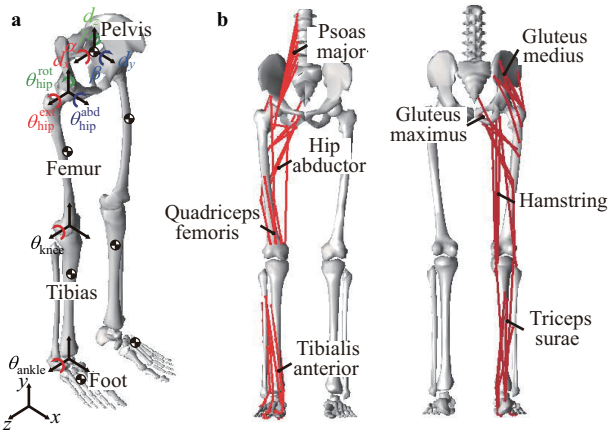


**Figure 2** Three-dimensional musculoskeletal gait model. **a** Joint DOF definition; **b** muscle bundles considered within the model.

As shown in Fig. 2b, we neglected the left limb muscles of the gait2392 model and reduced some internal ones. As a result, the muscle groups in our model were gluteus maximus, psoas major, gluteus medius, hip abductors, quadriceps femoris, hamstring, triceps surae, and tibialis anterior. The muscle path was determined using the fixed via point paths [66].

A Hill-type muscle model [67] was utilized to describe its force-generating capacities, see Fig. 3a. It consisted of three force elements: a contractile element (CE), representing the active muscle force produced by sarcomeres, a parallel-connected passive element (PE) corresponding to the passive stiffness within the muscle belly, and a passive elastic tendon element in series connection with CE and PE. The pennation angle $\alpha$, i.e., the angle between the muscle fiber direction and the tendon axis, was also included in the Hill-type model. For a pennated muscle, the contractile force $F_{\mathrm{CE}}^{\mathrm{mus}}$, passive muscle force $F_{\mathrm{PE}}^{\mathrm{mus}}$, and tendon force $F^{\mathrm{tend}}$ satisfied the following equilibrium equation:

$$\left(F_{\mathrm{CE}}^{\mathrm{mus}} + F_{\mathrm{PE}}^{\mathrm{mus}}\right)\cos\alpha = F^{\mathrm{tend}}. \tag{3}$$

The active contractile properties of the Hill-type muscle model were controlled by its fiber length $l^{\mathrm{mus}}$, fiber contraction velocity $\dot{l}^{\mathrm{mus}}$, and muscle activation $a(t)$. Muscle fibers contracted after being stimulated by motor neurons, and its activation level $a(t)$ reflected the proportion of the stimulated fibers to the total amount of the physiological cross-sectional area. As shown in Fig. 3a and b, the contractile force $F_{\mathrm{CE}}^{\mathrm{mus}}$ can be expressed as below:

$$F_{\mathrm{CE}}^{\mathrm{mus}} = a(t)F_0^{\mathrm{mus}} f_l\left(l^{\mathrm{mus}}, l_0^{\mathrm{mus}}\right) f_{\dot{l}}\left(\dot{l}^{\mathrm{mus}}, \dot{l}_0^{\mathrm{mus}}\right). \tag{4}$$

Here, $F_0^{\mathrm{mus}}$ is the maximum isometric force, $l_0^{\mathrm{mus}}$ corresponds to the optimum fiber length, and $\dot{l}_0^{\mathrm{mus}}$ is the maximum contractile velocity [68]. $f_l$ and $f_{\dot{l}}$ are the two functions representing the muscle force-length and force-velocity correlations, respectively [19, 68, 69].

$$f_l\left(l^{\mathrm{mus}}, l_0^{\mathrm{mus}}\right) = \exp\left\{-\left[\frac{9}{4}\left(\frac{l^{\mathrm{mus}}}{l_0^{\mathrm{mus}}} - \frac{19}{20}\right)\right]^4 - \left[\frac{9}{4}\left(\frac{l^{\mathrm{mus}}}{l_0^{\mathrm{mus}}} - \frac{19}{20}\right)\right]^2\right\}, \tag{5}$$

and

$$f_{\dot{l}}\left(\dot{l}^{\mathrm{mus}}, \dot{l}_0^{\mathrm{mus}}\right) = \begin{cases} 0, & -\dot{l}_0^{\mathrm{mus}} > \dot{l}^{\mathrm{mus}}, \\ -\dfrac{1}{\arctan(5)}\arctan\left(-5\dfrac{\dot{l}^{\mathrm{mus}}}{\dot{l}_0^{\mathrm{mus}}}\right)+1, & 0.2\dot{l}_0^{\mathrm{mus}} \ge \dot{l}^{\mathrm{mus}} \ge -\dot{l}_0^{\mathrm{mus}}, \\ \dfrac{\pi}{4\arctan(5)} + 1, & \dot{l}^{\mathrm{mus}} > 0.2\dot{l}_0^{\mathrm{mus}}. \end{cases} \tag{6}$$

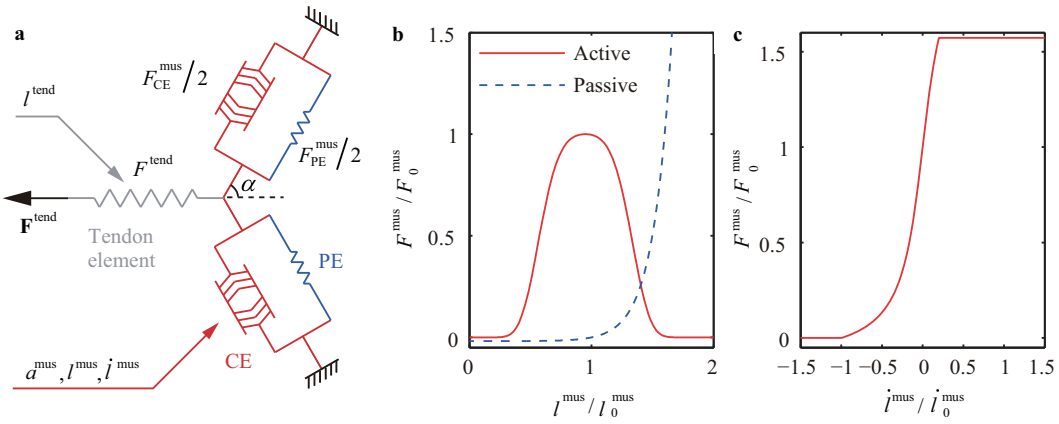


**Figure 3** Hill-type muscle model. **a** Equilibrium musculotendon model of a bipennate muscle; **b** muscle force-length curve; **c** muscle force-velocity curve.

The PE is independent of neuromuscular control. It starts to produce force when $l^{\text{mus}}$ is stretched beyond $l_0^{\text{mus}}$. The PE force $F_{\text{PE}}^{\text{mus}}$ is expressed as

$$F_{\text{PE}}^{\text{mus}} = \begin{cases} 0, & l_0^{\text{mus}} > l^{\text{mus}}, \\ 8F_0^{\text{mus}}\left(\dfrac{l^{\text{mus}}}{l_0^{\text{mus}}} - 1\right)^3, & 1.63l_0^{\text{mus}} \geq l^{\text{mus}} \geq l_0^{\text{mus}}, \\ 2F_0^{\text{mus}}, & l^{\text{mus}} > 1.63l_0^{\text{mus}}. \end{cases} \tag{7}$$

The tendon force $F^{\text{tend}}$ is nonlinear in the toe region ($\varepsilon \leq 2\varepsilon_0^{\text{tend}}$) and then linear with the stiffness $k^{\text{tend}}$. Therefore, the tendon force $F^{\text{tend}}$ can be expressed as [70]

$$F^{\text{tend}} = \begin{cases} 0, & 0 > \varepsilon, \\ \dfrac{k^{\text{tend}}}{4\varepsilon_0^{\text{tend}}}\varepsilon^2, & 2\varepsilon_0^{\text{tend}} \geq \varepsilon \geq 0, \\ k^{\text{tend}}(\varepsilon - \varepsilon_0^{\text{tend}}), & \varepsilon > 2\varepsilon_0^{\text{tend}}. \end{cases} \tag{8}$$

Here, the reference length of the tendon strain $\varepsilon$ is taken as the tendon slack length $l_0^{\text{tend}}$, i.e., $\varepsilon = 0.5[(l^{\text{tend}}/l_0^{\text{tend}})^2 - 1]$.

The governing equations of the musculoskeletal multibody system can be written as

$$\begin{aligned} &\boldsymbol{M}(\boldsymbol{q},t)\ddot{\boldsymbol{q}} - \boldsymbol{Q}(\boldsymbol{q},\dot{\boldsymbol{q}},\boldsymbol{a},t) + \boldsymbol{C}_{\boldsymbol{q}}^{\mathrm{T}}\boldsymbol{\lambda} = \boldsymbol{0}, \\ &\boldsymbol{C}(\boldsymbol{q},t) = \boldsymbol{0}, \\ &\tau_a(\boldsymbol{a},\boldsymbol{u})\dot{\boldsymbol{a}} - (\boldsymbol{u} - \boldsymbol{a}) = \boldsymbol{0}, \end{aligned} \tag{9}$$

where $\boldsymbol{M}$ is the system mass matrix, $\boldsymbol{q}$ is the vector of the generalized coordinates, and $\boldsymbol{Q}$ is the generalized force vector. The vector of the constraints of the whole system $\boldsymbol{C} = [\boldsymbol{C}_{\text{joint}}^{\mathrm{T}}, \boldsymbol{C}_{\text{mot}}^{\mathrm{T}}]^{\mathrm{T}}$ includes all anatomical joints $\boldsymbol{C}_{\text{joint}}$ and exerted motion constraints $\boldsymbol{C}_{\text{mot}}$, and $\boldsymbol{\lambda} = [\boldsymbol{\lambda}_{\text{joint}}^{\mathrm{T}}, \boldsymbol{\lambda}_{\text{mot}}^{\mathrm{T}}]^{\mathrm{T}}$ denotes its corresponding vector of the Lagrange multipliers. The muscle control vector $\boldsymbol{a}$ consists of the activation level of each muscle, and the vector $\boldsymbol{u}$ is composed of each muscular excitation.

## 2.3 Inverse kinematics

Based on the musculoskeletal model presented above, we first performed an inverse kinematics analysis using the measured infrared and virtual landmark positions, see Fig. 4a. Firstly, the anatomical landmarks embedded in the musculoskeletal model were located to correlate the gait kinematics with the bone segment positions. Their time-dependent coordinates were denoted as $\tilde{\boldsymbol{r}}_{\text{infra}}^i$ ($i = 1, 2, \cdots, N_{\text{infra}}$), $\tilde{\boldsymbol{r}}_{\text{AI}}^i$ ($i = 1, 2, \cdots, N_{\text{AI}}$), where $N_{\text{infra}}$ and $N_{\text{AI}}$ correspond to the number of landmarks obtained from infrared and markerless motion tracking systems, respectively. Considering the anatomical difference between the linear-scaled multibody model [63] and the actual human skeleton, together with the soft tissue elasticity [71], a spring-damper unit was introduced between each landmark measured by infrared $\boldsymbol{r}_{\text{infra}}^i$ and markerless motion capture systems $\boldsymbol{r}_{\text{AI}}^i$ and their corresponding anatomical positions:

$$\begin{aligned} \boldsymbol{Q}_{\text{infra}}^i &= -\left(k_{\text{infra}}\left\|\boldsymbol{r}_{\text{infra}}^i - \tilde{\boldsymbol{r}}_{\text{infra}}^i\right\| + c_{\text{infra}}\left\|\dot{\boldsymbol{r}}_{\text{infra}}^i - \dot{\tilde{\boldsymbol{r}}}_{\text{infra}}^i\right\|\right)\boldsymbol{n}, \\ \boldsymbol{Q}_{\text{AI}}^i &= -\left(k_{\text{AI}}\left\|\boldsymbol{r}_{\text{AI}}^i - \tilde{\boldsymbol{r}}_{\text{AI}}^i\right\| + c_{\text{AI}}\left\|\dot{\boldsymbol{r}}_{\text{AI}}^i - \dot{\tilde{\boldsymbol{r}}}_{\text{AI}}^i\right\|\right)\boldsymbol{n}. \end{aligned} \tag{10}$$

Here, $\boldsymbol{Q}_{\text{infra}}^i$ and $\boldsymbol{Q}_{\text{AI}}^i$ denote the viscoelastic force vectors induced by minimizing the tracking errors between the subject-specific motion capture data and the linear-scaled model, and $\boldsymbol{n}$ is the unit vector between the measured and the palpated landmarks. Equation (10) was endowed with two sets of stiffness-damping coefficients, i.e., $\{k_{\text{infra}} = 5 \times 10^6$ N/m, $c_{\text{infra}} = 5 \times 10^4$ N s/m$\}$, and $\{k_{\text{AI}} = 5 \times 10^5$ N/m, $c_{\text{AI}} = 5 \times 10^3$ N s/m$\}$, due to the spatial accuracy difference between two tracking systems (markerless tracking: in cm level; infrared tracking: in mm level). If the stiffness parameters were high enough, the kinetic energy of human locomotion and the potential energy generated by gravity and soft tissue stiffness can be ignored. By this means,

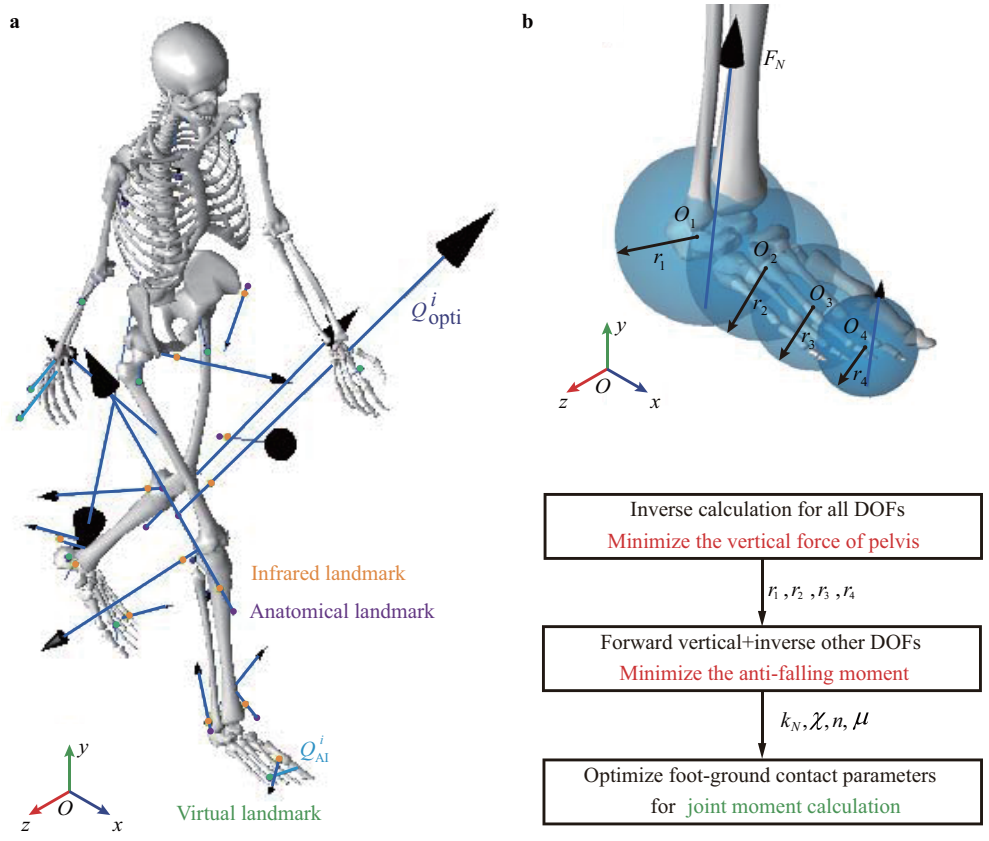


**Figure 4** Inverse kinematics and dynamics. **a** Inverse kinematics calculation via hybrid motion capture; **b** foot-ground contact parameter optimization.

Eq. (9) can be solved by the principle of minimum potential energy:

$$\min\ V = \sum_{i=1}^{N_{\text{infra}}} \left\| \boldsymbol{Q}^i_{\text{infra}} \right\|^2 + \sum_{i=1}^{N_{\text{AI}}} \left\| \boldsymbol{Q}^i_{\text{AI}} \right\|^2. \tag{11}$$

### 2.4 Inverse dynamics and foot-ground contact

The inverse kinematics approach took the vector of the joint angles $\boldsymbol{\theta}(t)$ and the vector of the muscle fiber lengths $\boldsymbol{L}^{\text{mus}} = \{l_1^{\text{mus}}, l_2^{\text{mus}}, \cdots, l_{N_{\text{mus}}}^{\text{mus}}\}^{\mathsf{T}}$ as model outputs. Here, $N_{\text{mus}}$ denotes the number of muscle bundles. Then, the moment arm can be expressed as [64]

$$\boldsymbol{R}^{\text{mus}} = \frac{\partial \boldsymbol{L}^{\text{mus}}}{\partial \boldsymbol{\theta}}. \tag{12}$$

The joint angles obtained from inverse kinematics calculations were then used as motion constraints:

$$\boldsymbol{C}_{\text{mot}} = \theta(\boldsymbol{q}) - \theta(t) = \boldsymbol{0}. \tag{13}$$

The obtained vector of the constraint equations constitutes part of the governing equations for inverse dynamics simulations:

$$\begin{aligned} &\boldsymbol{M}(\boldsymbol{q}, t)\ddot{\boldsymbol{q}} - \boldsymbol{Q}(\boldsymbol{q}, \dot{\boldsymbol{q}}, t) + \boldsymbol{C}_{\boldsymbol{q}}^{\mathsf{T}}\boldsymbol{\lambda} = \boldsymbol{0}, \\ &\boldsymbol{C}(\boldsymbol{q}, t) = [\boldsymbol{C}_{\text{joint}}^{\mathsf{T}}, \boldsymbol{C}_{\text{mot}}^{\mathsf{T}}]^{\mathsf{T}} = \boldsymbol{0}. \end{aligned} \tag{14}$$

Obviously, the mathematical form of Eq. (14) is identical to that of multibody mechanical systems. In other words, numerical simulation procedures developed based on machinery multibody systems [72-75] were also suitable for biodynamics simulations. The vector of the joint torques $\boldsymbol{M}_{\text{ID}}$ can be expressed based on the vector of the Lagrange multipliers associated with the motion constraints:

$$\boldsymbol{M}_{\text{ID}} = \left(\frac{\partial \theta}{\partial \boldsymbol{q}}\right)^{-\mathsf{T}} \left(\frac{\partial \boldsymbol{C}_{\text{mot}}}{\partial \boldsymbol{q}}\right)^{\mathsf{T}} \boldsymbol{\lambda}_{\text{mot}}. \tag{15}$$

In Eq. (14), the generalized force vector $\boldsymbol{Q}$ contains the effect of foot-ground contact force $F_N$ and friction force $F_\mu$. Without generality, a contact force model proposed by Flores et al. [76] which can characterize the energy dissipation behavior during foot-ground reactions was adopted in this study:

$$\begin{aligned} &F_N = k_N \delta^n + \chi \delta^n \dot{\delta}, \\ &\chi = \frac{8(1 - c_r)}{5 c_r \dot{\delta}_0}, \end{aligned} \tag{16}$$

where $k_N$ denotes the contact stiffness, $n$ is the nonlinear coefficient, $c_r$ is the restitution coefficient, and $\dot{\delta}_0$ corresponds

to the initial contact velocity. The universal form of the foot-ground friction force $F_\mu$ is written as

$$F_\mu = \mu(\boldsymbol{v}_T)F_N. \tag{17}$$

In general, the friction coefficient $\mu$ is a nonlinear function of the relative velocity $\boldsymbol{v}_T$ between the foot and the ground [77, 78]. For the sake of simplicity, we further assumed that the kinetic friction coefficient and the static one take the same value $\mu$. Therefore, the unknown parameters for the foot-ground contact model were $k_N$, $\chi$, $n$, $\mu$.

To describe the contact geometry of the foot sole, four viscoelastic contact spheres were arranged at geometric center of the calcaneus, cuneiform, metatarsal, and phalanges, see Fig. 4b. The initial value of each sphere radius $R_i$ ($i$ = 1, 2, 3, 4) was fitted by the generic bone geometry. To optimize the modeling parameters of the foot-ground contact, the following two-step optimization scheme was adopted:

(1) All joint angles were determined by inverse kinematics calculations without forward dynamics predictions. The parameter values of $k_N$, $\chi$, $n$, $\mu$ were taken from Shourijeh and McPhee [38] and remained unchanged, and the radius of each contact sphere $r_i$ was selected as the optimization variables. The biomechanical responses of human locomotion were then calculated by Eq. (15). The residual load corresponding to the pelvis vertical movement $F_{\text{vert}}$ was taken as the objective function. Its value should always be zero if the calculated foot-ground contact force was consistent with the real-world case.

(2) The optimized parameters of the contact geometry were kept unchanged in the following step. The pelvic movement constraint that determined its vertical motion was then released at this step, and the contact and friction force parameters ($k_N$, $\chi$, $n$, $\mu$) were taken as optimization variables. A time-dependent sagittal torque $M_{\text{sagit}}$ was exerted at the pelvic mass center to prevent falling. This value was selected as the objective function, since that $M_{\text{sagit}}$ should approximate zero when the contact model parameters were close to real-world situations.

## 2.5 FMIS analysis

As shown in Fig. 5, the resultant torque of each joint generated by its surrounding muscles was calculated via the inverse dynamics approach. Numerous simulations have shown that it is plausible to resolve the muscle redundancy problem according to the SO hypothesis while satisfying the dynamic equilibrium equation of each joint. However, the conventional SO approach cannot consider the muscle-tendon force equilibrium. The concept of FMIS framework [15] aims to release the dynamic equilibrium constraint by introducing the torque tracking errors into the objective function. However, a robust way to find the initial activa-

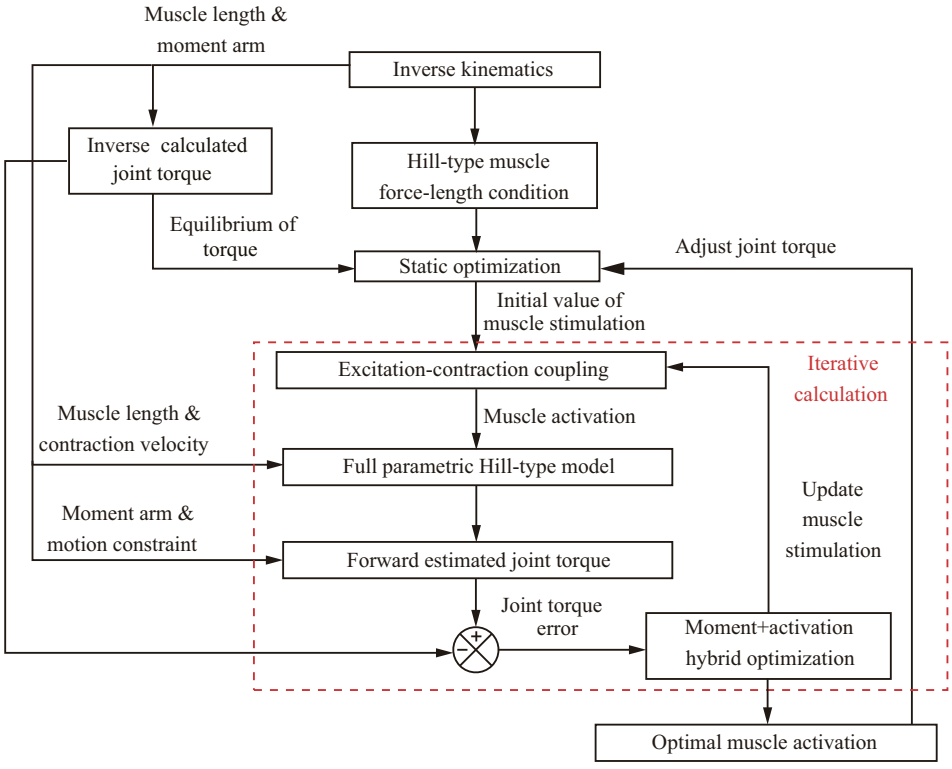


**Figure 5** FMIS dynamics framework.

tion values was in need to tackle the nonlinearities from the musculotendon equilibrium equation along with the muscle excitation-contraction coupling characteristics.

Firstly, it was assumed that the muscle activation patterns are only related to the current state of human locomotion and have nothing to do with their time histories [79]. Therefore, Eq. (9) was equivalent to a series of overdetermined equations. To speed up the computational efficiency of the FMIS method, the guess values of each muscle excitation were first obtained by solving a SO problem. By this means, the muscle forces were resolved by minimizing the sum of squared muscle excitation:

$$\min\ J_{\text{static}} = \sum_{i=1}^{N_{\text{mus}}} (w_i u_i)^2, \tag{18}$$

where the constraint functions were taken as

$$\begin{aligned} &\boldsymbol{R}^{\text{mus}}\boldsymbol{F}^{\text{mus}}(\boldsymbol{a}) = \boldsymbol{M}_{\text{ID}} + \Delta\boldsymbol{M}, \\ &\left(\frac{\partial\boldsymbol{\theta}}{\partial\boldsymbol{q}}\right)^{\mathrm{T}} \boldsymbol{M}_{\theta} = \boldsymbol{M}\ddot{\boldsymbol{q}} + \left(\frac{\partial\boldsymbol{C}}{\partial\boldsymbol{q}}\right)^{\mathrm{T}} \boldsymbol{\lambda} - \boldsymbol{Q}_{\text{ext}}, \\ &\boldsymbol{C}(\boldsymbol{q}, \dot{\boldsymbol{q}}, t) = \boldsymbol{0}, \\ &0.01 \le a_i \le 1,\ i = 1,\ 2, \cdots,\ N_{\text{mus}}. \end{aligned} \tag{19}$$

Here, $\boldsymbol{F}^{\text{mus}} = \{F_1^{\text{tend}},\ F_2^{\text{tend}}, \cdots,\ F_{N_{\text{mus}}}^{\text{tend}}\}^{\mathrm{T}}$ is the generalized musculotendon force vector, a nonlinear function of $\boldsymbol{a}$ according to Eq. (4), and $\Delta\boldsymbol{M}$ represents the controlling torque depended upon the torque tracking error.

The obtained excitation value of each muscle was then substituted into Eq. (3) to calculate the muscle fiber and tendon lengths. Afterward, the CE and PE forces can be calculated by Eqs. (4) and (7), respectively. The dynamic equilibrium constraint was then released to account for the time delay between the neural excitation and its corresponding muscular activation [80]. The muscle activation was used as an input to calculate the joint torque. Therefore, the objective function of the hybrid optimization problem was then expressed as

$$\min\ J_{\text{FMIS}} = (1-\gamma)\sum_{i=1}^{N_{\text{mus}}} (w_i a_i)^2 + \gamma \sum_{i=1}^{N_{\text{joint}}} (M_{\text{ID}} - M_{\text{FD}})^2, \tag{20}$$

where $\gamma$ is the weight of the joint torque, and $N_{\text{joint}}$ denotes the number of joints within the proposed model. The optimization problem is subjected to the following constraints:

$$\begin{aligned} &\boldsymbol{M}_{\text{FD}} = \boldsymbol{R}^{\text{mus}}\boldsymbol{F}^{\text{mus}}(\boldsymbol{a}), \\ &\left(\frac{\partial\boldsymbol{\theta}}{\partial\boldsymbol{q}}\right)^{\mathrm{T}} \boldsymbol{M}_{\text{ID}} = \boldsymbol{M}\ddot{\boldsymbol{q}} + \left(\frac{\partial\boldsymbol{C}}{\partial\mathrm{q}}\right)^{\mathrm{T}} \boldsymbol{\lambda} - \boldsymbol{Q}_{\text{ext}}, \\ &\boldsymbol{C}(\boldsymbol{q}, \dot{\boldsymbol{q}}, t) = \boldsymbol{0}, \\ &0.01 \le a_i \le 1,\ i = 1,\ 2, \cdots,\ N_{\text{mus}}. \end{aligned} \tag{21}$$

Then, a linear proportional feedback controller with the feedback gain $k_{\text{mom}} = 1$ was used to update $\Delta\boldsymbol{M}$:

$$\Delta\boldsymbol{M} = k_{\text{mom}}(\boldsymbol{M}_{\text{FD}} - \boldsymbol{M}_{\text{ID}}). \tag{22}$$

The musculoskeletal model was implemented based on our in-house code developed using C/C++ [19, 24, 69, 81]. The code expressing muscle contraction dynamics and solving activation optimization was produced using MATLAB R2020a (MathWorks, Inc., Natick, MA). All the simulations were performed on a 2.60-GHz, 64-bit laptop with 16 Gb of memory.

## 3. Results

Validation of the inverse kinematics results is shown in Fig. 6. The estimated sagittal angle based on the markerless motion capture system was correlated with infrared data ($R^2 = 0.96 \pm 0.05$). Here, the observed standard deviation of the hip flexion angle was generated by the variability of its baseline value. The hip abduction angle also showed a promising result ($R^2 = 0.82$). Using the landmarks from hybrid motion capture as inputs, the sagittal joint angles proposed by the multibody model agreed well with that measured by infrared motion capture ($R^2 = 0.97 \pm 0.03$). However, the hip adduction angle obtained from both methods shows a loose correlation ($R^2 = 0.60$) due to the mismatch between the real-world skeleton and the linear-scaled generic model.

The optimal geometrical and contact parameters are listed in Table 1. The viscosity coefficient of each contact sphere was taken from Shourijeh and McPhee [38], and the footground contact parameters of spheres 2 and 3 (see Fig. 4) were assumed identical for simplicity. The optimized contact stiffness of spheres 1 and 4 was one order of magnitude larger than the others because, during normal gait, the calcaneus and phalanges tend to withstand greater contact force than those of the cuneiform and metatarsal [82].

The obtained ground reaction forces over a gait cycle were then depicted in Fig. 7. Compared with the experimental data proposed in Ref. [40], the first peak of the estimated contact force was higher (see Fig. 7a) due to the sensitiveness of the contact detection method. Meanwhile, the estimated contact phase was shorter than the typical experimental data, which can attribute to the difference of the contact geometry between the sphere and the real-world plantar tissues [83]. As shown in Fig. 7b, the averaged horizontal force estimated based on a simple friction model was qualitatively in agreement with Lopes et al. [40].

We further compared the calculated joint torques based on different calculation methods, see Fig. 8. SO aims to satisfy the equilibrium of torque. However, by introducing the PE

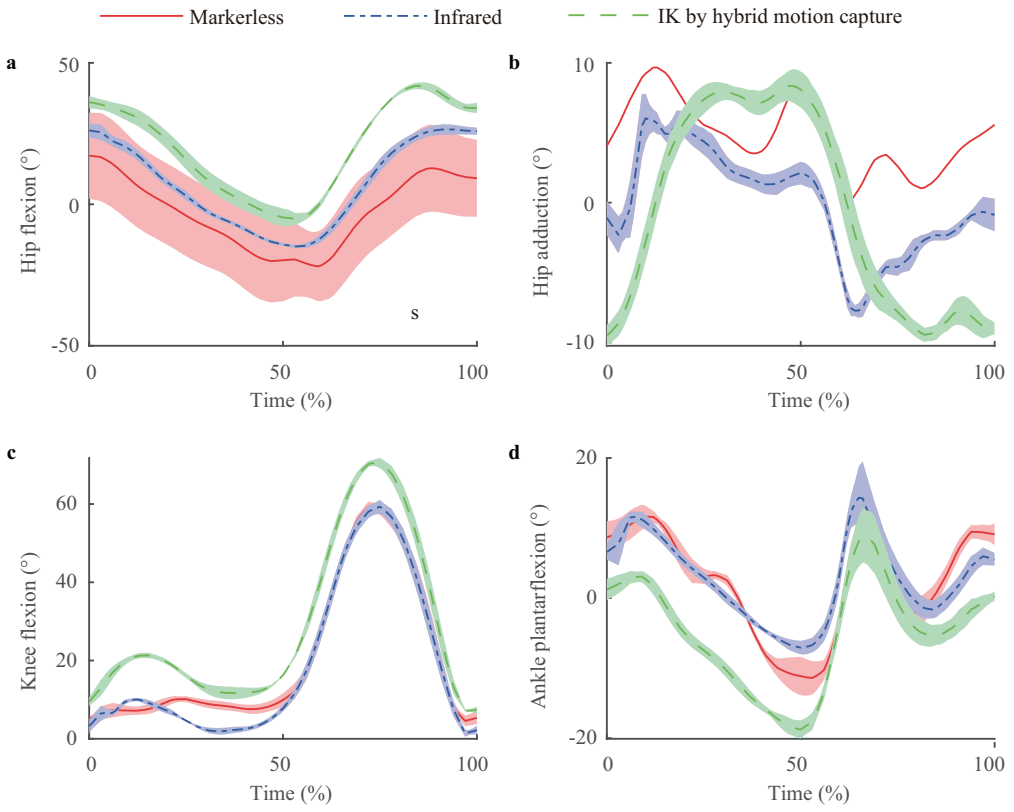


**Figure 6** Inverse kinematics calculation and its comparison with motion capture data. **a** Hip flexion-extension; **b** hip adduction-abduction; **c** knee flexion-extension; **d** ankle dorsiflexion-plantarflexion. IK = inverse kinematics.

**Table 1** Optimal foot-ground contact parameters

| Parameter | | Initial value | Lower bound | Upper bound | Optimal value |
|---|---|---|---|---|---|
| Geometry | $R_1$ (mm) | 64 | 44 | 84 | 73.6 |
| | $R_2$ (mm) | 58 | 38 | 78 | 62.8 |
| | $R_3$ (mm) | 61 | 41 | 81 | 51.9 |
| | $R_4$ (mm) | 30 | 27 | 67 | 42.1 |
| Contact stiffness | $k_{N1}$ (N m) | $9.8 \times 10^3$ | $9.8 \times 10^1$ | $9.8 \times 10^5$ | $9.46 \times 10^5$ |
| | $k_{N2} = k_{N3}$ (N m) | $2.2 \times 10^3$ | $2.2 \times 10^1$ | $2.2 \times 10^5$ | $4.57 \times 10^4$ |
| | $k_{N4}$ (N m) | $6.6 \times 10^3$ | $6.6 \times 10^1$ | $6.6 \times 10^5$ | $3.52 \times 10^5$ |
| Nonlinear coefficient | $n_1$ | 0.93 | 0.50 | 2.50 | 2.07 |
| | $n_2 = n_3$ | 0.95 | 0.50 | 2.50 | 2.41 |
| | $n_4$ | 0.89 | 0.50 | 2.50 | 1.87 |
| Friction coefficient | $\mu_1$ | 0.33 | 0.10 | 0.75 | 0.13 |
| | $\mu_2 = \mu_3$ | 0.41 | 0.10 | 0.75 | 0.10 |
| | $\mu_4$ | 0.45 | 0.10 | 0.75 | 0.12 |

force, the obtained hip abduction (Fig. 8b) and ankle torques (Fig. 8d) generated non-negligible errors. The FMIS procedure with a full parametric Hill-type model can largely reduce the joint torque error by imposing the torque tracking algorithm.

Meanwhile, the FMIS algorithm can largely alternate the recruitment patterns of the lower limb muscles, see Fig. 9. Compared with the EMG observations, the SO along with FMIS schemes can qualitatively capture the activation characteristics of the gluteus medius, biceps femoris, and tibialis anterior muscles. However, the SO approach cannot accurately obtain the activation patterns of bi-articular muscles like the rectus femoris and gastrocnemius. In comparison, considering the musculotendon equilibrium equations regardless of muscle paths, the FMIS approach successfully captured the activations of the rectus femoris at mid-stance. The passive dorsiflexion ankle stiffness led to the gastrocnemius activation in the swing phase of gait, in agreement with

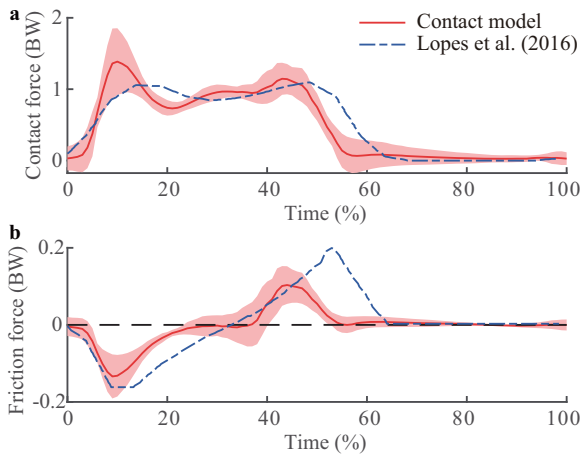


**Figure 7** Calculation of estimated foot-ground reaction forces during a gait cycle normalized by the body weight (BW) and comparison with experimental measurements proposed by Lopes et al. [40]. Here, the shaded regions indicate the ±1 standard deviation of the experimental data. **a** Vertical component; **b** horizontal component.

the EMG observations. Moreover, compared with the excitation results only taking the Hill-type force-length condition into account, the activation patterns predicted by FMIS were strongly alternated by introducing the tendon stiffness and the muscle contraction dynamics.

## 4. Discussion

Kinematics and kinetic analysis of human gait rely on reliable motion capture data. According to our validation results (see Fig. 6), the markerless motion capture system can obtain reliable joint angles. However, only two virtual landmarks within a body segment were identified based on deep convolutional neural networks. Therefore, the three-dimensional joint angles should be calculated based on some simplifications [57, 58], and the estimated landmark positions cannot directly drive the three-dimensional musculoskeletal model. However, the hybrid motion capture system can improve the accuracy of inverse kinematics results by adding virtual markers to the original Helen Haynes marker set. Automatic identification of anatomic landmarks also reduced the time for preparing the gait test.

Accurate kinematic measurement provided a solid foundation for the parameter identification of the foot-ground contact model. Foot-ground reaction forces were usually measured via force plates or plantar pressure sensors. However, the force plate is not portable enough to be utilized in sports or rehabilitation conditions, and the insole sensor system cannot measure the friction between the foot and floor. Unlike other foot-ground contact modeling methods [43, 84], the

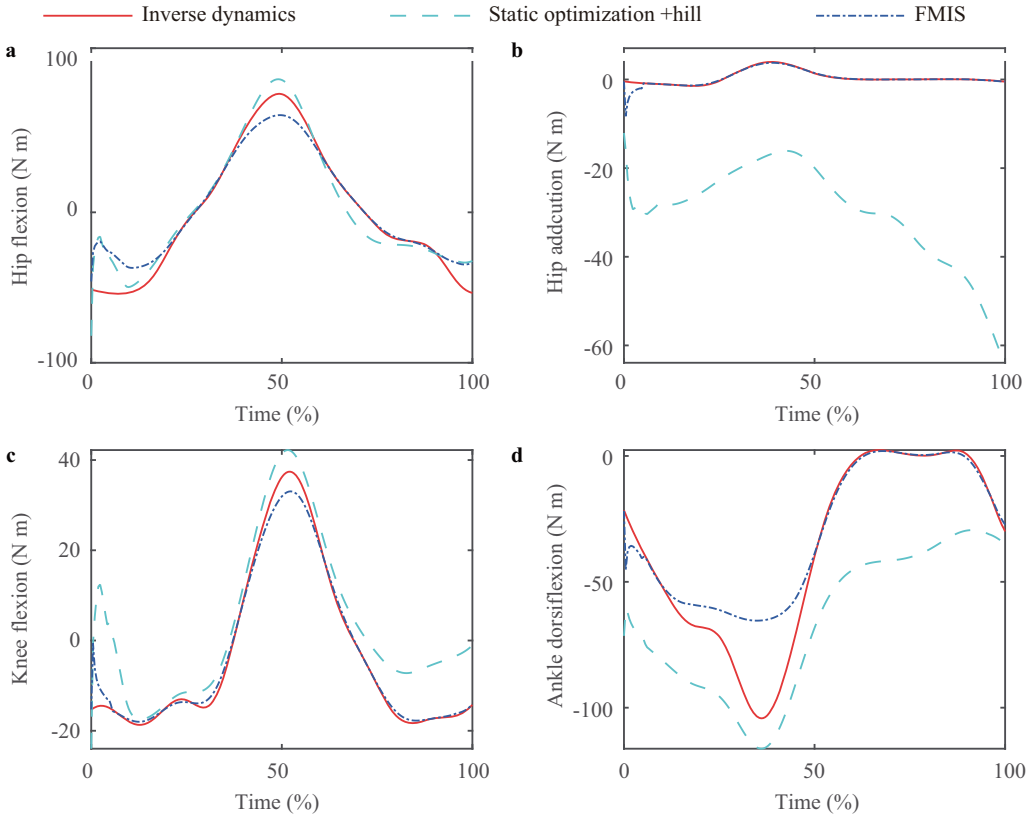


**Figure 8** Comparison of the joint torque results during a gait cycle. **a** Hip flexion (+) /extension (-); **b** hip adduction (+) / abduction (-); **c** knee flexion (+) / extension (-); **d** ankle dorsiflexion (+) / plantarflexion (-).

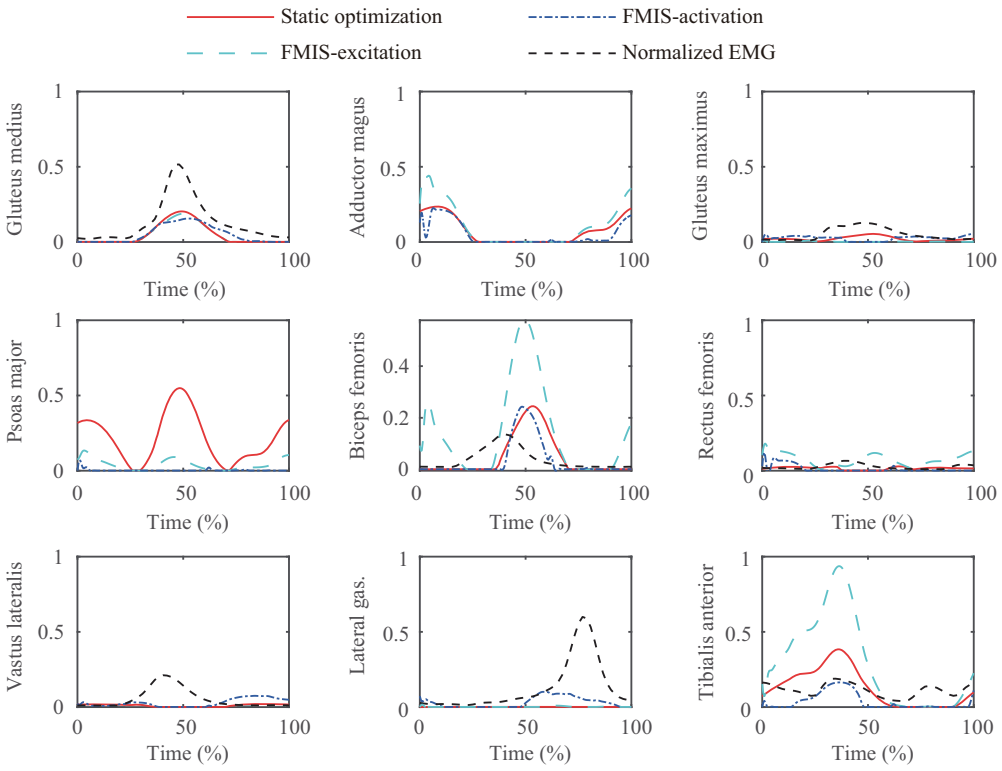


**Figure 9** Estimated muscle activations of the lower limb during a gait cycle. Gas. = gastrocnemius.

proposed parameter identification methods did not need any knowledge in priori. Moreover, the two-step optimization scheme successfully reduced the sensitivity of the estimated contact parameters. Further studies could introduce some information such as the spatiotemporal gait parameters to improve the accuracy of the estimated reaction forces.

In this study, the FMIS framework took the nonlinearities of muscle dynamics into account. Conventional musculoskeletal modeling frameworks, such as OpenSim and Anybody, tended to neglect the passive properties of individual muscles in SO analysis. However, this assumption could result in huge errors in the estimated joint loading [85,86]. Our simulation further demonstrates that the SO method overestimated the ankle torque (Fig. 8d) and overlooked the gastrocnemius activations without the passive stiffness (Fig. 9). The FMIS framework was also compatible with the deformation of tendon by implementing the musculotendon equilibrium equation [87]. The time delay induced by muscle activation dynamics, which has been proved crucial to the simulation results [88], can be considered within the proposed method. The basic idea of the proposed FMIS method is similar to the inverse-forward dynamics optimization method [21], but the current approach does not need to perform forward musculoskeletal simulations at each time step.

Compared with other forward dynamics approaches like CMC [20, 34] or FSO [36], the FMIS approach was more robust and reliable since the movements of bone segments were driven by kinematic measurements rather than muscle forces. As shown in Fig. 8d, the FMIS procedure predicted a non-negligible error of ankle plantarflexion torque during the terminal stance phase, which means that the dynamic balance equation of the ankle joint cannot be satisfied. Under this condition, the CMC and FSO methods depending on trajectory tracking tend to be divergent without introducing artificial joint torque actuators [89]. Moreover, the optimization methods based on trajectory tracking often used the higher derivatives of the measured landmark positions [20, 28, 34], whereas the virtual landmark positions estimated by deep neural networks were often highly oscillated. The proposed framework only needs the position signal as kinematic inputs. The oscillatory patterns of the landmark positions can be filtered by the damper force in Eq. (10).

However, some limitations are worth noting. Firstly, the sample size was limited to only one subject with repeated gait analysis. More locomotive tasks could be performed to compare the performance between FMIS and other forward-inverse coupling methods. Then, to quantitatively verify the estimated foot-ground reaction forces, the force plate measurements should be performed synchronously with the motion capture analysis. Next, the activation patterns of the muscles crossing the knee were not consistent with the EMG measurements. Muscle synergies [90, 91] could be intro-

duced into the optimization framework to improve the correlation between the estimated activation patterns with the real-world data. Moreover, many modeling parameters, such as the muscle insertion sites and optimal fiber lengths, were not subject-specific. Last but not least, the study only investigated the healthy gait with self-selected speed. Other typical human postures (i.e., standing, squatting) and daily activities (i.e., running, cursing) could be further investigated to validate our modeling and simulation procedures.

## 5. Conclusion

In this paper, a forward-inverse modeling framework was established to estimate joint torques and muscle activations in the lower extremity. The markerless motion capture system accurately predicted the sagittal lower limb kinematics, and the hybrid kinematic measurement approach reduced the number of attached markers. The proposed parameter identification method successfully estimated the foot-ground reaction forces without a priori knowledge. Compared with SO, the FMIS framework reduced the errors of hip adduction and ankle plantarflexion moments by introducing passive muscle stiffness. Implementation of the equilibrium musculotendon model together with the muscle contraction dynamics alternated the estimated bi-articular muscle activations during gait. The computational procedure of the current framework was hard to diverge by constraining joint kinematics using the measured data, which seems to be suitable for analyzing complex human movements such as athletic sports and rehabilitation exercises. Moreover, without using acceleration data as control inputs, the proposed framework can be potentially used in any multibody simulation software.

***Author contributions*** *Xinyue Wang designed the research, set up the experiment set-up, processed the numerical and experiment data, and wrote the first draft of the manuscript. Jianqiao Guo helped designed the research, set up the simulation set-up, and helped organize the manuscript. Jianqiao Guo and Qiang Tian revised and edited the final version.*

***Acknowledgements*** *This work was supported by the National Natural Science Foundations of China (Grant Nos. 12102035 and 12125201), the China Postdoctoral Science Foundation (Grant No. 2020TQ0042), and the Beijing Natural Science Foundation (Grant No. L212008). The authors would like to thank Yi Qu for his technical support and Prof. Gexue Ren for his helpful discussion of this paper.*

1 M. Ezati, B. Ghannadi, and J. McPhee, A review of simulation methods for human movement dynamics with emphasis on gait, Multibody Syst. Dyn. **47**, 265 (2019).
2 A. J. van den Bogert, M. Hupperets, H. Schlarb, and B. Krabbe, Predictive musculoskeletal simulation using optimal control: Effects of added limb mass on energy cost and kinematics of walking and running, Proc. Inst. Mech. Eng. Part P-J. Sports Eng. Tech. **226**, 123 (2012).
3 C. Zhang, X. Meng, D. E. Anderson, W. Wang, X. Tao, and B. Cheng, Effects of stretch reflex on back muscle response during sinusoidal whole body vibration in sitting posture: A model study, Int. J. Ind. Ergonomics **71**, 103 (2019).
4 X. Ma, J. Xu, H. Fang, Y. Lv, and X. Zhang, Adaptive neural control for gait coordination of a lower limb prosthesis, Int. J. Mech. Sci. **215**, 106942 (2022).
5 S. Barman, Y. Xiang, R. Rakshit, and J. Yang, Joint fatigue-based optimal posture prediction for maximizing endurance time in box carrying task, Multibody Syst. Dyn. **55**, 323 (2022).
6 Y. Guo, X. Zhang, M. An, and W. Chen, Determination of quadriceps forces in squat and its application in contact pressure analysis of knee joint, Acta Mech. Solid Sin. **25**, 53 (2012).
7 Y. Wang, L. Wang, C. Du, Z. Mo, and Y. Fan, A comparative study on dynamic stiffness in typical finite element model and multi-body model of C6-C7 cervical spine segment, Int. J. Numer. Meth. Biomed. Eng. **32**, e02750 (2016).
8 X. Liu, H. Huang, S. Ren, Q. Rong, and Y. Ao, Use of the normalcy index for the assessment of abnormal gait in the anterior cruciate ligament deficiency combined with meniscus injury, Comput. Meth. Biomech. Biomed. Eng. **23**, 1102 (2020).
9 L. Wang, X. Ding, W. Feng, Y. Gao, S. Zhao, and Y. Fan, Biomechanical study on implantable and interventional medical devices, Acta Mech. Sin. **37**, 875 (2021).
10 W. Wang, D. Wang, A. Falisse, P. Severijns, T. Overbergh, L. Moke, L. Scheys, F. De Groote, and I. Jonkers, A dynamic optimization approach for solving spine kinematics while calibrating subject-specific mechanical properties, Ann. Biomed. Eng. **49**, 2311 (2021).
11 W. Schiehlen, On the historical development of human walking dynamics, in: The History of Theoretical, Material and Computational Mechanics-Mathematics Meets Mechanics and Engineering, (Springer, Berlin, Heidelberg, 2014), pp. 101-116.
12 J. Rasmussen, M. Damsgaard, and M. Voigt, Muscle recruitment by the min/max criterion—a comparative numerical study, J. Biomech. **34**, 409 (2001).
13 M. P. T. Silva, and J. A. C. Ambrósio, Multibody Syst. Dyn. **8**, 219 (2002).
14 M. Ackermann, and A. J. van den Bogert, Optimality principles for model-based prediction of human gait, J. Biomech. **43**, 1055 (2010).
15 M. S. Shourijeh, K. B. Smale, B. M. Potvin, and D. L. Benoit, A forward-muscular inverse-skeletal dynamics framework for human musculoskeletal simulations, J. Biomech. **49**, 1718 (2016).
16 S. R. Hamner, A. Seth, K. M. Steele, and S. L. Delp, A rolling constraint reproduces ground reaction forces and moments in dynamic simulations of walking, running, and crouch gait, J. Biomech. **46**, 1772 (2013).
17 D. G. Lloyd, and T. F. Besier, An EMG-driven musculoskeletal model to estimate muscle forces and knee joint moments in vivo, J. Biomech. **36**, 765 (2003).
18 S. S. Razu, and T. M. Guess, Electromyography-driven forward dynamics simulation to estimate in vivo joint contact forces during normal, smooth, and bouncy gaits, J. Biomech. Eng. **140**, 071012 (2018).
19 J. Guo, H. Huang, Y. Yu, Z. Liang, J. Ambrósio, Z. Zhao, G. Ren, and Y. Ao, Modeling muscle wrapping and mass flow using a mass-variable multibody formulation, Multibody Syst. Dyn. **49**, 315 (2020).
20 D. G. Thelen, and F. C. Anderson, Using computed muscle control to generate forward dynamic simulations of human walking from experimental data, J. Biomech. **39**, 1107 (2006).
21 A. Asadi Nikooyan, H. E. J. Veeger, E. K. J. Chadwick, M. Praagman, and F. C. T. van der Helm, Development of a comprehensive musculoskeletal model of the shoulder and elbow, Med. Biol. Eng. Comput. **49**, 1425 (2011).
22 M. Kia, A. P. Stylianou, and T. M. Guess, Evaluation of a musculoskeletal model with prosthetic knee through six experimental gait trials, Med. Eng. Phys. **36**, 335 (2014).
23 R. S. Razavian, N. Mehrabi, and J. McPhee, A neuronal model of central pattern generator to account for natural motion variation, J. Com-

put. Nonlinear Dyn. **11**, 021007 (2016).
24 J. Guo, W. Guo, and G. Ren, Embodiment of intra-abdominal pressure in a flexible multibody model of the trunk and the spinal unloading effects during static lifting tasks, Biomech. Model. Mechanobiol. **20**, 1599 (2021).
25 F. C. Anderson, and M. G. Pandy, Static and dynamic optimization solutions for gait are practically equivalent, J. Biomech. **34**, 153 (2001).
26 F. De Groote, A. L. Kinney, A. V. Rao, and B. J. Fregly, Evaluation of direct collocation optimal control problem formulations for solving the muscle redundancy problem, Ann. Biomed. Eng. **44**, 2922 (2016).
27 M. Sharif Shourijeh, and J. McPhee, Forward dynamic optimization of human gait simulations: A global parameterization approach, J. Comput. Nonlinear Dyn. **9**, 031018 (2014).
28 T. Yamasaki, K. Idehara, and X. Xin, Estimation of muscle activity using higher-order derivatives, static optimization, and forward-inverse dynamics, J. Biomech. **49**, 2015 (2016).
29 M. Skipper Andersen, M. de Zee, M. Damsgaard, D. Nolte, and J. Rasmussen, Introduction to force-dependent kinematics: Theory and application to mandible modeling, J. Biomech. Eng. **139**, 091001 (2017).
30 X. Zhang, Z. Chen, L. Wang, W. Yang, D. Li, and Z. Jin, Prediction of hip joint load and translation using musculoskeletal modelling with force-dependent kinematics and experimental validation, Proc. Inst. Mech. Eng. H **229**, 477 (2015).
31 Z. Chen, Z. Zhang, L. Wang, D. Li, Y. Zhang, and Z. Jin, Evaluation of a subject-specific musculoskeletal modelling framework for load prediction in total knee arthroplasty, Med. Eng. Phys. **38**, 708 (2016).
32 X. Meng, A. G. Bruno, B. Cheng, W. Wang, M. L. Bouxsein, and D. E. Anderson, Incorporating six degree-of-freedom intervertebral joint stiffness in a lumbar spine musculoskeletal model—method and performance in flexed postures, J. Biomech. Eng. **137**, 1010081 (2015).
33 H. Diao, H. Xin, J. Dong, X. He, D. Li, and Z. Jin, Prediction of cervical spinal joint loading and secondary motion using a musculoskeletal multibody dynamics model via force-dependent kinematics approach, Spine **42**, E1403 (2017).
34 D. G. Thelen, F. C. Anderson, and S. L. Delp, Generating dynamic simulations of movement using computed muscle control, J. Biomech. **36**, 321 (2003).
35 M. Wesseling, L. C. Derikx, F. de Groote, W. Bartels, C. Meyer, N. Verdonschot, and I. Jonkers, Muscle optimization techniques impact the magnitude of calculated hip joint contact forces, J. Orthop. Res. **33**, 430 (2015).
36 M. S. Shourijeh, N. Mehrabi, and J. McPhee, Forward static optimization in dynamic simulation of human musculoskeletal systems: A proof-of-concept study, J. Comput. Nonlinear Dyn. **12**, 051005 (2017).
37 R. Pàmies-Vilà, J. M. Font-Llagunes, U. Lugrís, and J. Cuadrado, Parameter identification method for a three-dimensional foot-ground contact model, Mech. Mach. Theor. **75**, 107 (2014).
38 M. S. Shourijeh, and J. McPhee, Foot-ground contact modeling within human gait simulations: From Kelvin-Voigt to hyper-volumetric models, Multibody Syst. Dyn. **35**, 393 (2015).
39 M. Ezati, P. Brown, B. Ghannadi, and J. McPhee, Comparison of direct collocation optimal control to trajectory optimization for parameter identification of an ellipsoidal foot-ground contact model, Multibody Syst. Dyn. **49**, 71 (2020).
40 D. S. Lopes, R. R. Neptune, J. A. Ambrósio, and M. T. Silva, A superellipsoid-plane model for simulating foot-ground contact during human gait, Comput. Methods Biomech. Biomed. Eng. **19**, 954 (2016).
41 T. W. Dorn, Y. C. Lin, and M. G. Pandy, Estimates of muscle function in human gait depend on how foot-ground contact is modelled, Comput. Methods Biomech. Biomed. Eng. **15**, 657 (2012).
42 J. N. Jackson, C. J. Hass, and B. J. Fregly, Development of a subject-specific foot-ground contact model for walking, J. Biomech. Eng. **138**, 091002 (2016).
43 R. Van Hulle, C. Schwartz, V. Denoël, J. L. Croisier, B. Forthomme, and O. Brüls, A foot/ground contact model for biomechanical inverse dynamics analysis, J. Biomech. **100**, 109412 (2020).
44 S. Corazza, L. Mündermann, A. M. Chaudhari, T. Demattio, C. Cobelli, and T. P. Andriacchi, A markerless motion capture system to study musculoskeletal biomechanics: Visual hull and simulated annealing approach, Ann. Biomed. Eng. **34**, 1019 (2006).
45 S. Skals, K. P. Rasmussen, K. M. Bendtsen, J. Yang, and M. S. Andersen, A musculoskeletal model driven by dual Microsoft Kinect Sensor data, Multibody Syst. Dyn. **41**, 297 (2017).
46 Y. Hirano, D. Kushida, and H. Matsumoto, in Contactless motion analysis system using a kinect and musculoskeletal model: Proceedings of 2017 IEEE Life Sciences Conference, (IEEE, Piscataway, 2017), pp. 308-311.
47 M. Eltoukhy, C. Kuenze, M. S. Andersen, J. Oh, and J. Signorile, Prediction of ground reaction forces for Parkinson's disease patients using a kinect-driven musculoskeletal gait analysis model, Med. Eng. Phys. **50**, 75 (2017).
48 L. Wade, L. Needham, P. McGuigan, and J. Bilzon, Applications and limitations of current markerless motion capture methods for clinical gait biomechanics, PeerJ **10**, e12995 (2022).
49 R. M. Kanko, E. Laende, W. S. Selbie, and K. J. Deluzio, Inter-session repeatability of markerless motion capture gait kinematics, J. Biomech. **121**, 110422 (2021).
50 R. M. Kanko, E. K. Laende, G. Strutzenberger, M. Brown, W. S. Selbie, V. DePaul, S. H. Scott, and K. J. Deluzio, Assessment of spatiotemporal gait parameters using a deep learning algorithm-based markerless motion capture system, J. Biomech. **122**, 110414 (2021).
51 R. M. Kanko, E. K. Laende, E. M. Davis, W. S. Selbie, and K. J. Deluzio, Concurrent assessment of gait kinematics using marker-based and markerless motion capture, J. Biomech. **127**, 110665 (2021).
52 D. R. Burnett, N. H. Campbell-Kyureghyan, R. V. Topp, and P. M. Quesada, Biomechanics of lower limbs during walking among candidates for total knee arthroplasty with and without low back pain, Biomed Res. Int. **2015**, 1 (2015).
53 M. Andriluka, L. Pishchulin, P. Gehler, and B. Schiele, in 2d human pose estimation: New benchmark and state of the art analysis: Proceedings of the IEEE Conference on computer Vision and Pattern Recognition, (IEEE, Piscataway, 2014), pp. 3686-3693.
54 E. D'Antonio, J. Taborri, E. Palermo, S. Rossi, and F. Patanè, in A markerless system for gait analysis based on openpose library: Proceedings of 2020 IEEE International Instrumentation and Measurement Technology Conference (I2MTC), (IEEE, Piscataway, 2020), pp. 1-6.
55 K. Sun, B. Xiao, D. Liu, and J. Wang, in Deep high-resolution representation learning for human pose estimation: Proceedings of the IEEE/CVF Conference on Computer Vision and Pattern Recognition, 2019, pp. 5693-5703.
56 J. A. Zeni Jr, J. G. Richards, and J. S. Higginson, Two simple methods for determining gait events during treadmill and overground walking using kinematic data, Gait Posture **27**, 710 (2008).
57 H. Liu, S. Leigh, and B. Yu, Sequences of upper and lower extremity motions in javelin throwing, J. Sports Sci. **28**, 1459 (2010).
58 H. Liu, S. Leigh, and B. Yu, Comparison of sequence of trunk and arm motions between short and long official distance groups in javelin throwing, Sports Biomech. **13**, 17 (2014).
59 C. Quental, J. Folgado, J. Ambrósio, and J. Monteiro, A multibody biomechanical model of the upper limb including the shoulder girdle, Multibody Syst. Dyn. **28**, 83 (2012).
60 D. G. Thelen, Adjustment of muscle mechanics model parameters to simulate dynamic contractions in older adults, J. Biomech. Eng. **125**, 70 (2003).
61 A. Seth, J. L. Hicks, T. K. Uchida, A. Habib, C. L. Dembia, J. J. Dunne, C. F. Ong, M. S. DeMers, A. Rajagopal, M. Millard, S. R. Hamner, E. M. Arnold, J. R. Yong, S. K. Lakshmikanth, M. A. Sherman, J. P. Ku, and S. L. Delp, OpenSim: Simulating musculoskeletal dynamics and neuromuscular control to study human and animal movement, PLoS Comput. Biol. **14**, e1006223 (2018).
62 A. Kłodowski, T. Rantalainen, A. Mikkola, A. Heinonen, and H.

Sievänen, Flexible multibody approach in forward dynamic simulation of locomotive strains in human skeleton with flexible lower body bones, Multibody Syst. Dyn. **25**, 395 (2011).
63 M. E. Lund, M. S. Andersen, M. de Zee, and J. Rasmussen, Scaling of musculoskeletal models from static and dynamic trials, Int. Biomech. **2**, 1 (2015).
64 G. T. Yamaguchi, Dynamic Modeling of Musculoskeletal Motion: A Vectorized Approach for Biomechanical Analysis in Three Dimensions, (Springer Science & Business Media, Dordrecht, 2005).
65 K. Amankwah, R. Triolo, R. Kirsch, and M. Audu, A model-based study of passive joint properties on muscle effort during static stance, J. Biomech. **39**, 2253 (2006).
66 S. L. Delp, J. P. Loan, M. G. Hoy, F. E. Zajac, E. L. Topp, and J. M. Rosen, An interactive graphics-based model of the lower extremity to study orthopaedic surgical procedures, IEEE Trans. Biomed. Eng. **37**, 757 (1990).
67 F. E. Zajac, Muscle and tendon: Properties, models, scaling, and application to biomechanics and motor control, Crit. Rev. Biomed. Eng. **17**, 359 (1989).
68 M. P. T. Silva, and J. A. C. Ambrósio, Solution of redundant muscle forces in human locomotion with multibody dynamics and optimization tools, Mech. Based Des. Struct. Mach. **31**, 381 (2003).
69 J. Guo, Y. Sun, Y. Hao, L. Cui, and G. Ren, A mass-flowing muscle model with shape restrictive soft tissues: correlation with sonoelastography, Biomech. Model. Mechanobiol. **19**, 911 (2020).
70 L. Blankevoort, and R. Huiskes, Ligament-bone interaction in a three-dimensional model of the knee, J. Biomech. Eng. **113**, 263 (1991).
71 S. Guitteny, Y. Lafon, V. Bonnet, R. Aissaoui, and R. Dumas, Dynamic estimation of soft tissue stiffness for use in modeling socket, orthosis or exoskeleton interfaces with lower limb segments, J. Biomech. **134**, 110987 (2022).
72 J. Xiong, N. Wang, and C. Liu, Bicycle dynamics and its circular solution on a revolution surface, Acta Mech. Sin. **36**, 220 (2020).
73 M. Jiang, X. Rui, W. Zhu, F. Yang, and Y. Zhang, Optimal design of 6-DOF vibration isolation platform based on transfer matrix method for multibody systems, Acta Mech. Sin. **37**, 127 (2021).
74 W. Yao, L. Yang, and M. Guo, Gauss optimization method for the dynamics of unilateral contact of rigid multibody systems, Acta Mech. Sin. **37**, 494 (2021).
75 Z. Yu, and Y. Cui, New ANCF solid-beam element: Relationship with Bézier volume and application on leaf spring modeling, Acta Mech. Sin. **37**, 1318 (2021).
76 P. Flores, M. Machado, M. T. Silva, and J. M. Martins, On the continuous contact force models for soft materials in multibody dynamics, Multibody Syst. Dyn. **25**, 357 (2011).
77 L. Yu, Z. Zhao, J. Tang, and G. Ren, Integration of absolute nodal elements into multibody system, Nonlinear Dyn. **62**, 931 (2010).
78 F. F. Zhuang, and Q. Wang, Modeling and analysis of rigid multibody systems with driving constraints and frictional translation joints, Acta Mech. Sin. **30**, 437 (2014).
79 C. Quental, J. Folgado, and J. Ambrósio, A window moving inverse dynamics optimization for biomechanics of motion, Multibody Syst. Dyn. **38**, 157 (2016).
80 D. A. Winter, Biomechanics and Motor Control of Human Movement (John Wiley & Sons, Waterloo, 2009).
81 J. Guo, J. Chen, J. Wang, G. Ren, Q. Tian, and C. Guo, EMG-assisted forward dynamics simulation of subject-specific mandible musculoskeletal system, J. Biomech. **139**, 111143 (2022).
82 M. W. Whittle, Gait Analysis: An Introduction (Butterworth-Heinemann, Oxford, 2014).
83 Y. Luximon, A. Luximon, J. Yu, and M. Zhang, Biomechanical evaluation of heel elevation on load transfer—experimental measurement and finite element analysis, Acta Mech. Sin. **28**, 232 (2012).
84 K. J. H. Ngoh, D. Gouwanda, A. A. Gopalai, and Y. Z. Chong, Estimation of vertical ground reaction force during running using neural network model and uniaxial accelerometer, J. Biomech. **76**, 269 (2018).
85 C. Y. Scovil, and J. L. Ronsky, Sensitivity of a Hill-based muscle model to perturbations in model parameters, J. Biomech. **39**, 2055 (2006).
86 R. M. Byrne, A. K. Aiyangar, and X. Zhang, Sensitivity of musculoskeletal model-based lumbar spinal loading estimates to type of kinematic input and passive stiffness properties, J. Biomech. **102**, 109659 (2020).
87 M. Millard, T. Uchida, A. Seth, and S. L. Delp, Flexing computational muscle: Modeling and simulation of musculotendon dynamics, J. Biomech. Eng. **135**, 021005 (2013).
88 K. Stollenmaier, W. Ilg, and D. F. B. Haeufle, Predicting perturbed human arm movements in a neuro-musculoskeletal model to investigate the muscular force response, Front. Bioeng. Biotechnol. **8**, 308 (2020).
89 B. Odle, J. Reinbolt, G. Forrest, and T. Dyson-Hudson, Construction and evaluation of a model for wheelchair propulsion in an individual with tetraplegia, Med. Biol. Eng. Comput. **57**, 519 (2019).
90 E. Chiovetto, B. Berret, I. Delis, S. Panzeri, and T. Pozzo, Investigating reduction of dimensionality during single-joint elbow movements: A case study on muscle synergies, Front. Comput. Neurosci. **7**, 11 (2013).
91 R. Sharif Razavian, N. Mehrabi, and J. McPhee, A model-based approach to predict muscle synergies using optimization: Application to feedback control, Front. Comput. Neurosci. **9**, 121 (2015).

# 人体肌肉骨骼多体系统的正逆向耦合动力学建模方法

王心悦, 郭建峤, 田强

**摘要** 人体步态的肌骨系统多体动力学建模已被证实在探讨肌骨系统损伤的病理机制等方面具有重要意义. 然而, 传统的逆动力学分析方法需输入外力传感器测量数据, 无法兼顾骨骼肌的非线性动力学特征. 此外, 正向动力学方法往往计算量很大, 仅能够应用在相对简单的分析工况中. 本文提出了一种肌骨系统仿真方法, 实现无力台条件下的足-地面力估计, 并在肌肉力计算中兼顾肌腱弹性与优化控制策略. 我们结合基于红外相机的贴点动作捕捉与基于深度神经网络的无标记动作捕捉系统, 实现对受试者下肢运动的同步测量. 足-地面相互作用力通过一类软物质接触力模型求得, 接触参数通过两步优化方法辨识得到. 肌肉发力模式首先通过静态优化算法求解, 得到的肌肉激活度作为后续正逆向耦合仿真的初值. 进一步, 我们采用一种力矩跟踪方法, 通过调整肌肉激活度, 使基于肌肉-肌腱内力平衡方程求得的关节力矩与逆动力学解算得到的关节力矩间误差最小. 为验证本文提出的计算方法的正确性, 将仿真求得的肌肉激活度与一名健康受试者实测表面肌电进行比较. 本文提出的仿真方法为人体关节力矩、肌肉-肌腱内力、以及肌肉激活模式提出了一种可靠的求解方法, 能够增进对健康人与患者步态生物力学的理解.